



Laser-Assisted Growth of *t*-Te Nanotubes and their Controlled Photo-induced Unzipping to ultrathin core-Te/sheath-TeO₂ Nanowires

Thomas Vasileiadis^{1,2}, Vassileios Dracopoulos¹, Mary Kollia³ & Spyros N. Yannopoulos^{1,2}

¹Foundation for Research and Technology Hellas – Institute of Chemical Engineering Sciences (FROTH/ICE-HT), P.O. Box 1414, GR-26504, Rio-Patras, Greece, ²Department of Materials Science, University of Patras, GR-26504, Rio-Patras, Greece, ³Lab of Electron Microscopy and Microanalysis, University of Patras, GR-26504, Rio-Patras, Greece.

One dimensional (1D) nanostructures of semiconducting oxides and elemental chalcogens culminate over the last decade in nanotechnology owing to their unique properties exploitable in several applications sectors. Whereas several synthetic strategies have been established for rational design of 1D materials using solution chemistry and high temperature evaporation methods, much less attention has been given to the laser-assisted growth of hybrid nanostructures. Here, we present a laser-assisted method for the controlled fabrication of Te nanotubes. A series of light-driven phase transition is employed to controllably transform Te nanotubes to core-Te/sheath-TeO₂ and/or even neat TeO₂ nanowires. This solid-state laser-processing of semiconducting materials apart from offering new opportunities for the fast and spatially controlled fabrication of anisotropic nanostructures, provides a means of simultaneous growing and integrating these nanostructures into an optoelectronic or photonic device.

One dimensional (1D) inorganic nanostructures, namely, nanowires (NWs) and nanotubes (NTs) represent today a mature and fertile field in nanoscience and nanotechnology. Apart from the fundamental interest in understanding phenomena at the nanoscale, a variety of applications are foreseen in photonics, microelectronics, energy conversion, and the biomedical sector^{1–4}. Besides the well-established and thoroughly studied classical 1D structures², i.e. CNTs, ZnO and Si NWs, other elemental materials, such as the chalcogens Se and Te, exhibit strong tendency to form NWs and NTs¹. In contrast to Sulfur, which forms eight-membered crown-like rings (due to the preference of the *cis* conformation), Se and Te crystallize in the trigonal (*t*-) form consisting of long polymeric helical chains (*trans* conformation) of covalently bonded atoms, with three atoms as the repeat unit. The chains arrange in hexagonal packing interacting via van der Waals forces. Inter-chain interactions are stronger in *t*-Te in comparison to *t*-Se chains. The chain-like structure of the *t*-Te and *t*-Se building blocks, ultimately justifies their tendency to grow in anisotropic 1D structures. Furuta *et al.* were the first who studied the kinetics of vapor-grown *t*-Te whiskers more than forties year ago⁵.

Up until now, two established methods are mostly employed for the controlled synthesis of 1D *t*-Te nanostructures; solution chemistry^{6–11} and vapor deposition at high temperature^{12–16}. While many interesting properties, including photoconductivity, photoelectricity, thermoelectricity, piezoelectricity, and nonlinear optical response, characterize bulk *t*-Te, a number of other important applications have recently been reported for *t*-Te nanostructures. These include ammonia gas sensors at room temperature¹⁷, Hg(II) sensor in aqueous media¹⁸, conversion of graphite oxide to graphenic leaf-like structures¹⁹, and antibacterial activity better than silver nanoparticles, while maintaining their toxicity lower than silver's²⁰. Besides their interesting properties, *t*-Te nanostructures have also been used as templates to fabricate 1D nanostructures of other materials²¹. Given this context, it is obvious that nanostructured *t*-Te is becoming an emerging functional material. Despite the long body of experimental work on *t*-Te nanostructures, only few studies have been focused on the growth of TeO₂ NWs. The first growth of TeO₂ NWs was achieved through heating Te nanostructures, in the presence of oxygen, at high temperature (500 °C) for about 20 min²². TeO₂ NWs were found to exhibit room temperature gas sensing properties^{23,24} and enhanced luminescence when covered by a layer of ZnO²⁵. In addition, TeO₂ is a promising optical material that meets several applications in laser devices, optical fibers, and non-linear optics.

SUBJECT AREAS:

NANOWIRES

ELECTRONIC DEVICES

SURFACES, INTERFACES AND THIN FILMS

OPTICAL MATERIALS

Received
8 November 2012

Accepted
2 January 2013

Published
4 February 2013

Correspondence and requests for materials should be addressed to S.N.Y. (sny@iceht.forth.gr)



Unlike the existing investigations to fabricate *t*-Te 1D nanostructures, which require hazardous chemicals (e.g. hydrazine solutions) and elaborate high temperature processes, here we demonstrate a novel, photo-processing method of bulk *t*-Te that leads to the fast, one step, controlled fabrication of *t*-Te NTs. These nanostructures grow by irradiating bulk elemental Te with visible continuous wave lasers either under inert atmosphere or at ambient conditions for short exposure times. The presence of oxygen controls the ripping of *t*-Te NTs, via photo-oxidation, towards the formation of ultrathin core-Te/sheath-TeO₂ NWs, which takes place in the course of longer irradiation. In the present work, Te, Te/TeO₂ and TeO₂ nanostructures are fabricated by visible cw lasers (441.6, 488.0, and 514.5 nm) and characterized by Raman scattering, Field Emission Scanning Electron Microscopy (FESEM), energy dispersive spectroscopy (EDS) and high resolution transmission electron microscopy (HRTEM). Raman scattering provided key *in-situ* information on the microscopic origin of the involved photo-induced phase changes. Schematic diagrams of the experimental set-up for selective and large-area growth of nanostructures are shown in Figure S1.

Results

Figure 1 presents the surface morphology of laser-processed (pre-polished) bulk Te at different irradiation times using a low power density, D1 (see Methods). The focused laser beam spot is in the present case of about 1–2 μm in diameter and its effect on the Te surface morphology becomes more prominent with increasing exposure time. The central part of the photo-processed area acquires gradually a smooth texture (images A1, B1, C1), while

nanostructuring is observed at the periphery of this area (images A2, B2, C2) where light fluence is lower. Raman spectra shown in the rightmost part of Figure 1 (A3, B3, C3) can help identifying the atomic-scale changes in the course of irradiation. For comparison we show the Raman spectrum of bulk *t*-Te (lines with dots), which was recorded with even smaller power density (D2) over a short accumulation time in order to avoid photo-induced changes. The Raman spectrum of *t*-Te exhibits two bands at 124 and 144 cm⁻¹, which originate from vibrational modes of the long helical chains with A₁ and E_{TO} symmetries, respectively²⁶. The intensity of the 124 cm⁻¹ band appears here weaker than that of the 144 cm⁻¹ one due to the effect of the instrument notch filter. What is impressively revealed by the Raman spectra is the development of a broad continuum spectrum which signifies the emergence of *amorphous* TeO₂ phase. To support this conclusion, the Raman spectrum of the bulk glassy TeO₂²⁷ is presented in B3 for comparison. EDS microanalysis (Figure S2) confirms the presence of TeO₂ in the center of the irradiated area. In addition, a new band at ~165 cm⁻¹ appears whose intensity grows systematically with irradiation time. This band can be assigned to *amorphous* tellurium, a-Te, indicating that photo-induced disordering of the helical chains in *t*-Te takes place.

At longer exposure times, the morphology of the irradiated area does not change appreciable (images C1, C2). However, the Raman spectra (C3) indicate *phase change* effects. Amorphous TeO₂ crystallizes in the γ-TeO₂ polymorph²⁷ in about 15 min of continuous irradiation for the specific light fluence used (D1). This polymorph is not a typical crystalline phase of TeO₂; however, it has been reported²⁷ as the crystallized product after heat treatment of bulk glassy TeO₂. The present findings demonstrate that the γ-phase is

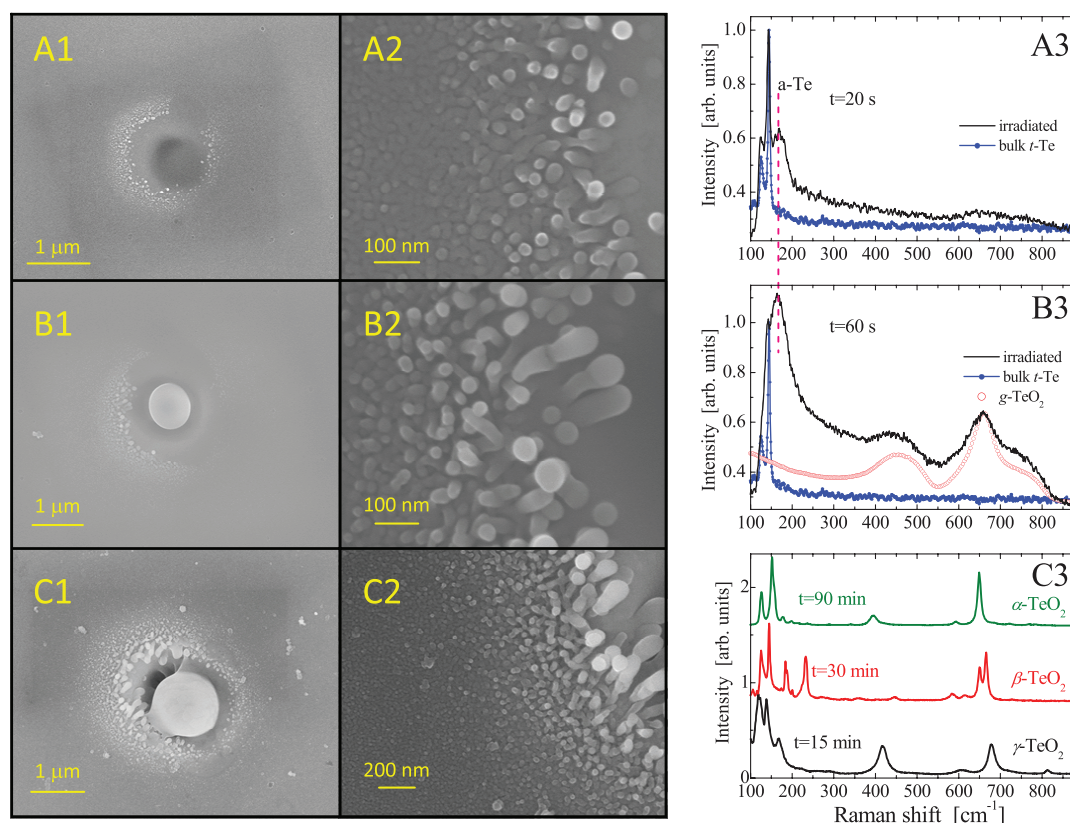


Figure 1 | Time dependence of photo-induced nanostructuring of *t*-Te surfaces at low light fluence ($D1 = 10^4 \text{ W cm}^{-2}$). FESEM images in A, B, and C correspond to irradiation times 20 s, 40 s, and 30 min, respectively. A1, B1, C1: low magnification FESEM images of the irradiated area. A2, B2, C2: high magnification FESEM images at the periphery of the irradiated area. Rightmost figures: Raman spectra of the pre-irradiated (lines with dots/blue curves) and post-irradiated surfaces (solid/black curves) are shown in A3 and B3. The Raman spectrum of glassy TeO₂ is shown in B3 for comparison. C3 illustrates Raman spectra of long-term irradiation. Amorphous TeO₂ crystallizes to γ-TeO₂, which sequentially transforms to β-TeO₂ (tellurite) and α-TeO₂ (para-tellurite) in the course of irradiation.



metastable and transforms to the crystalline structure of the well-known tellurite mineral, β -TeO₂ rather rapidly after its formation as long as the crystal is exposed. Another phase transition at even longer irradiation times leads finally to the para-tellurite crystal, α -TeO₂. Concluding, light drives the initially photo-oxidized amorphous a-TeO₂ to a multiplicity of crystalline phases including the mineral tellurite whose laboratory growth has not yet been reported.

Exposure of *t*-Te to intense light, by increasing the fluence by one order of magnitude, leads to mass transport through material ablation. Under intense irradiation a pluralism of nanostructures emerges controlled by exposure time. Photo-processing the surface in this way results in a crater formation and the growth of nanostructures takes place at the borders and outside the crater through a vapor-solid process. In the areas where nanostructures grow, light intensity is appreciably smaller than the intensity at the central region, albeit not negligible considering the Gaussian laser beam profile and the size of the crater. Therefore, the nanostructures created by the abrupt ablation, still remain under (weak) illumination as long as the laser is kept on. Representative FESEM images are shown in Figure 2. At short irradiation times (3 s, Figure 2A) nanopatterning of the surface is observed; anisotropic 1D structures with small aspect ratio are evident. These hexagonal-shaped particle act as nucleation seeds for the incoming vapors which lead to the formation of *t*-Te nanotubes, following the growth mechanism described below. Indeed, increasing the irradiation time leads to the formation of bundled Te nanotubes (45 s, Figure 2B, C). In their majority, the inner diameter of these *t*-Te NTs are of about 30 to 60 nm, while their

length is still short, i.e. in the sub-micrometer scale. Exposure at even longer times (60–90 s) leads to the formation of longer *t*-Te NTs such as those shown in Figure 2 D, E. These nanostructures have the morphology of the corresponding *t*-Te NTs reported in the literature. However, our laser-assisted grown *t*-Te NTs exhibit appreciably smaller inner diameters than those reported elsewhere using both solution chemistry and high temperature thermal evaporation^{1,10,13,16}, where the reported inner diameters exceed the scale of 100 nm. At longer exposure times, 1–2 min, we observe that the initially smooth surface of *t*-Te NTs (Figure 2D) acquires a nanostructured roughness (Figure 2E). The textured surface signifies the onset of photo-induced oxidation of *t*-Te to a-TeO₂ via the mechanism revealed by Raman scattering (Fig. 1).

Prolonged exposure to laser light (3–4 min) leads to enhanced photo-oxidation. TeO₂ nanoparticles act as molecular scissors which lead to a progressive fraying of Te nanotubes to thinner nanowires. Evidence for this photo-damage mechanism of *t*-Te NTs to Te/TeO₂ or TeO₂ nanowires is shown clearly in Figure 2F and in more detail in Figure 2G. The NW diameters range from 10 to 30 nm. TeO₂ nanowires formed by the ripping of *t*-Te NTs after adequate irradiation are crystalline, as is demonstrated by Raman scattering (Figure 1 C3 spectrum of α -TeO₂). The situation is simpler when the laser assisted growth of *t*-Te NTs takes place under inert atmosphere (in the presence of argon gas). In that case, only *t*-Te NTs of the morphology shown in Figure 2H are found even at long exposure (5 min). Similar nanostructures grow irrespectively of the exposure time (see Figure S3). Irradiation experiments under pure oxygen conditions revealed

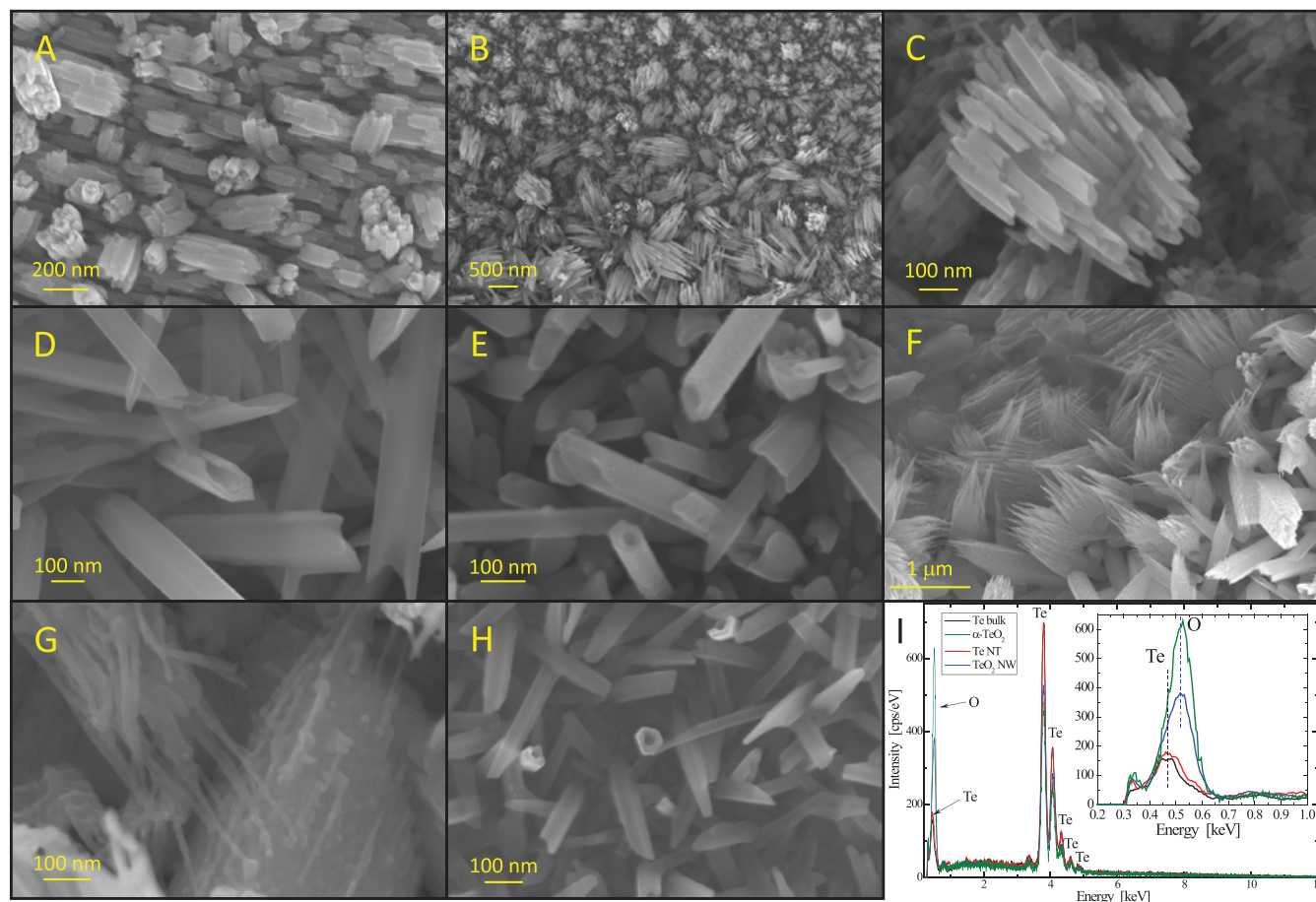


Figure 2 | Laser-assisted growth of *t*-Te and TeO₂ nanostructures at high light fluence ($D0 = 10^5 \text{ W cm}^{-2}$). FESEM images from A to D correspond to progressive increasing irradiation times from 3 s to 120 s. E shows nanostructured roughness due to surface oxidation. F and G illustrate NT ripping due to prolonged photo-oxidization. Neat *t*-Te NTs grow under argon atmosphere, image H, even at long irradiation times (5 min). EDS spectra of *t*-Te NTs, TeO₂ NWs, and bulk untreated *t*-Te and TeO₂ crystals are shown in I. The inset shows the low energy peaks in detail.



qualitatively similar nanostructure morphologies to those obtained at ambient conditions.

Photo-oxidation of the NTs takes place radially proceeding from the exposed surfaces, both inner and outer, to the depth of the NT wall. Depending on the exposure conditions photo-oxidation can be either complete or partial. In the latter case, the nanowire will consist of Te NW core surrounded by TeO₂ sheath. EDS analysis shown in Figure 2I provides support to the laser-assisted fabrication of *t*-Te NTs and their photo-transformation to TeO₂ NWs. The inset shows an enlargement of the low energy peak where both O and Te contribute. Bulk, unprocessed *t*-Te and *t*-Te NTs exhibit indistinguishable EDS patterns, while analysis of EDS data for the NWs show that in this particular case, 80% of the material consist of TeO₂ with the rest 20% being Te core, thus indicating incomplete photo-oxidation.

The effects reported above, observed using the 441.6 nm (2.81 eV) wavelength, are not specific to this photon energy. Experiments conducted using two other visible wavelengths, i.e. the 514.5 nm (2.41 eV) and 488.0 nm (2.54 eV) show consistent results for the formation of *t*-Te nanotubes. Their photo-oxidation to nanostructures containing TeO₂ is also demonstrated with these wavelengths, showing the generality of the photo-induced effects described above. Details of photo-processed nanostructures with the 2.41 and 2.54 eV photon energies are presented in Figure S4, where it is shown that in some cases *t*-Te NTs of 20 nm inside diameter and ~6 nm wall thickness are observed.

The reproducibility of the nanostructures morphology with various visible photon energies is not surprising for elemental Te, which is a low bandgap semiconductor ($E_g \approx 0.33$ eV) and a moderately low melting point solid ($T_m = 459^\circ\text{C}$). Visible or near-infrared lasers, whose energies appreciably exceed the E_g of *t*-Te, will have similar effects on the nanostructuring effects. An estimate of the ablation efficiency achieved with visible wavelength lasers can be obtained considering the absorption of elemental Te at various energies. To elucidate some details of the laser ablation mechanism the penetration depths $\mu_i = \lambda_i/4\pi k$, for the irradiation wavelengths λ_i used, were calculated based on the wavelength-dependent absorption coefficient k (complex refractive index) of Te²⁸. Since absorption depends on the relative orientation between the single crystal and the electric field and given that we start from polycrystalline samples, we can only provide upper (electric field \perp to *c* axis) and lower (electric field \parallel to *c* axis) limits for the penetration depth. Using the values $k^\perp = 3.63$ and $k^\parallel = 4.42$ for $\lambda = 441.6$ nm, $k^\perp = 3.76$ and $k^\parallel = 4.85$ for $\lambda = 488.0$ nm, and $k^\perp = 3.77$ and $k^\parallel = 5.08$ for $\lambda = 514.5$ nm, the estimated penetration depths are in the range 8–11 nm for all the above photon energies. These common ablation conditions reveal that the same mechanism describes the Te NTs growth; this is in harmony with the observed morphology of the nanostructures fabricated using different photon energies. The small penetration depth

entails absorption of considerable power into a small material volume. A rough estimation shows that for the current experimental conditions the temperature of the irradiated volume can rise to temperatures near the boiling point of Te. At these temperatures Te has appreciable vapor pressures, which accounts for the high yield and rapid formation of *t*-Te NTs via sublimation and condensation of the vapors around the irradiated area. Details about the various melting mechanisms (athermal and thermal) of elemental Te using ultrafast pulsed lasers can be found elsewhere²⁹.

Discussion

Before discussing the photo-induced oxidation of Te it would be instructive to briefly describe the Te NT growth mechanism. This has been discussed elsewhere for tubes grown either by solution-phase synthesis³⁰ or by thermal evaporation¹³. In the case of thermal evaporation it has been considered that supersaturation of Te vapors plays an important role, analogous to the concentration of Te atoms in the solution-phase synthesis. In brief, condensation of Te vapors leads to the creation of crystallites with hexagonal shape, which is dictated by the symmetry of the crystal lattice of Te. These crystallites act as nucleation centers for the Te atoms that condensate at the circumference of the seeds, driven by the free energy minimization requirement. High mobility of Te atoms is essential for their localization to the periphery of the hexagonal crystal. Indeed, Figure 3 (left panel) provides direct evidence of the initial steps of the Te nanotube growth. The white arrows show the surfaces of the hexagonal crystallites, perpendicular to the [0001] direction, that has originally grown, and which provides the template for incoming atoms to form the nanotube. A schematic diagram of the process is shown in Figure 3 (right panel).

Raman spectra collected *in situ* at different exposure intervals can help identifying the atomic-scale origin of the observed photo-induced oxidation. Key feature is the appearance in the Raman spectra of bands related to *amorphous* Te, a-Te, and amorphous TeO₂. The vibrational band attributed here to a-Te, situated at ~ 165 cm⁻¹ is blue-shifted in comparison to the vibrational modes of *t*-Te, in accordance to findings in a-Te prepared by vapor deposition³¹. The higher energy of the a-Te intra-chain vibrational mode in relation to its crystalline counterpart, originates from the weaker inter-chain interactions in a-Te, which causes strengthening of the intra-chain vibrations. This effect is also observed in the isomorphous crystalline and glassy Se^{32,33}. These findings demonstrate that the nanostructuring of the surface at low light fluence and short times originates from the combination of two photo-induced effects, i.e. *photo-induced amorphization* and *photo-oxidation* of *t*-Te (see Figure S5). It is still not certain if photo-induced amorphization precedes, or commences in parallel, to photo-oxidation. Given the above context, it might not be surprising that *t*-Te belonging to the family of the

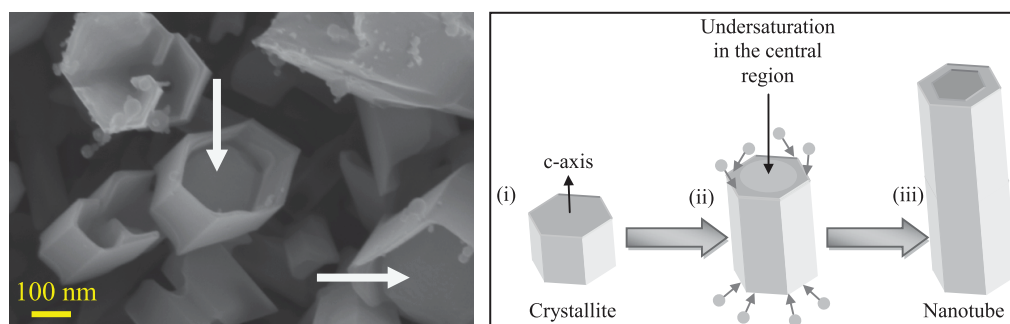


Figure 3 | Growth mechanism of *t*-Te nanotubes. Left: FESEM image of *t*-Te nanotubes at the initial growth stage. Right: Schematic illustration of the growth mechanism. (i) Condensation of vapors creates crystallites with hexagonal shape. (ii) Crystal growth takes place preferentially along the *c* axis of the crystal (owing to the highly anisotropic *t*-Te crystal lattice) and especially at the edge of the hexagonal planes where the free energy is higher. (iii) If the mobility of Te atoms is high enough, hollow nanotubes, instead of nanowires or nanorods, are formed.



light sensitive chalcogens³⁴, is susceptible to photo-induced amorphization and photo-oxidation.

The present findings demonstrate an all-laser, two-step method for the controlled fabrication of TeO₂ and/or core-Te/sheath-TeO₂ NWs. In the first step, a *bottom-up* process, i.e. the vapor-solid mechanism, underlies the very fast growth of *t*-Te NTs. In the second more complex step, a *top-down* process ensues where controlled exposure to near-UV light leads to the ripping of *t*-Te NTs to TeO₂ ultrathin nanowires through a solid-state photolytic reaction. Typical snapshots of the material's morphology in the course of the second step are depicted in Figure 4. Depending on the exposure conditions, the composition of the grown NWs can vary from purely TeO₂ under prolonged irradiation to core-Te/sheath-TeO₂ structures in the case of partial oxidation (see also Table S1). The central inset in Figure 4 provides a pictorial description of the tube-to-wire photo-induced ripping.

TEM and HRTEM images provide additional direct evidence about the crystallinity of *t*-Te NTs and the details of the core-Te/sheath-TeO₂ nanostructures. Representative TEM and HRTEM images are illustrated in Figure 5. The edge (open end) of a *t*-Te NT is shown in 5(A). The corresponding high magnification (HRTEM micrograph) in 5(B) demonstrates a lattice-resolved image with lattice planes marked with the white lines. Three typical *t*-Te planes are resolved with interplanar spacings of 0.59, 0.38, and 0.32 nm, which correspond to (001), (100) and (101), respectively. Another example of a single crystalline *t*-Te nanowire is shown in the HRTEM image in 5(C). This NW is single crystalline in nature and has grown in the [0001] direction. Image 5(D) shows a magnified TEM image a core/sheath nanowire with diameter of ~35 nm and

aspect ratio of ~25. The inset in 5(D) depicts the entire NW. A more transparent layer (TeO₂) covers the whole surface of the NW; the limits of the outer surface of the sheath layer are denoted by the arrows. Finally, a HRTEM image of a core-Te/sheath-TeO₂ NW is shown in 5(E). This image reveals the crystalline nature of the dark area which represents *t*-Te, while the thin amorphous (grey) layer of about 5 nm in thickness, which denotes TeO₂, is evidently amorphous. This finding agrees with Raman scattering data that have demonstrated the non-crystalline nature of the TeO₂ phase at the early stages of irradiation.

There are several merits associated with the described method; some of the main ones are the following. (i) The process is fast and environmentally friendly in that no hazardous substances are used and no post-fabrication treatment is needed to remove chemical byproducts, thus resulting in high purity nanostructures. (ii) The method enables the feasibility of using focused laser beams for selectively inscribing NW/NT patterns of elemental Te and/or TeO₂ on the surface of pre-deposited Te films, thus providing a means of simultaneous growth and integrating the nanostructures into an optoelectronic or photonic device. (iii) Photo-oxidation of *t*-Te NTs yields ultrathin TeO₂ NWs in contrast to those formed by thermal evaporation^{23–25} whose thickness is in the range of 70–100 nm or larger. Apart from well documented properties of TeO₂ NWs, e.g. room temperature gas sensing, enhanced luminescence and non-linear optical properties, using the method reported here and controlling the extent of photo-induced oxidation may affect other photo-induced changes of such hybrid semiconducting materials³⁵. In addition, the coexistence of two nanostructured materials in contact with contrasting optical and electrical properties may be

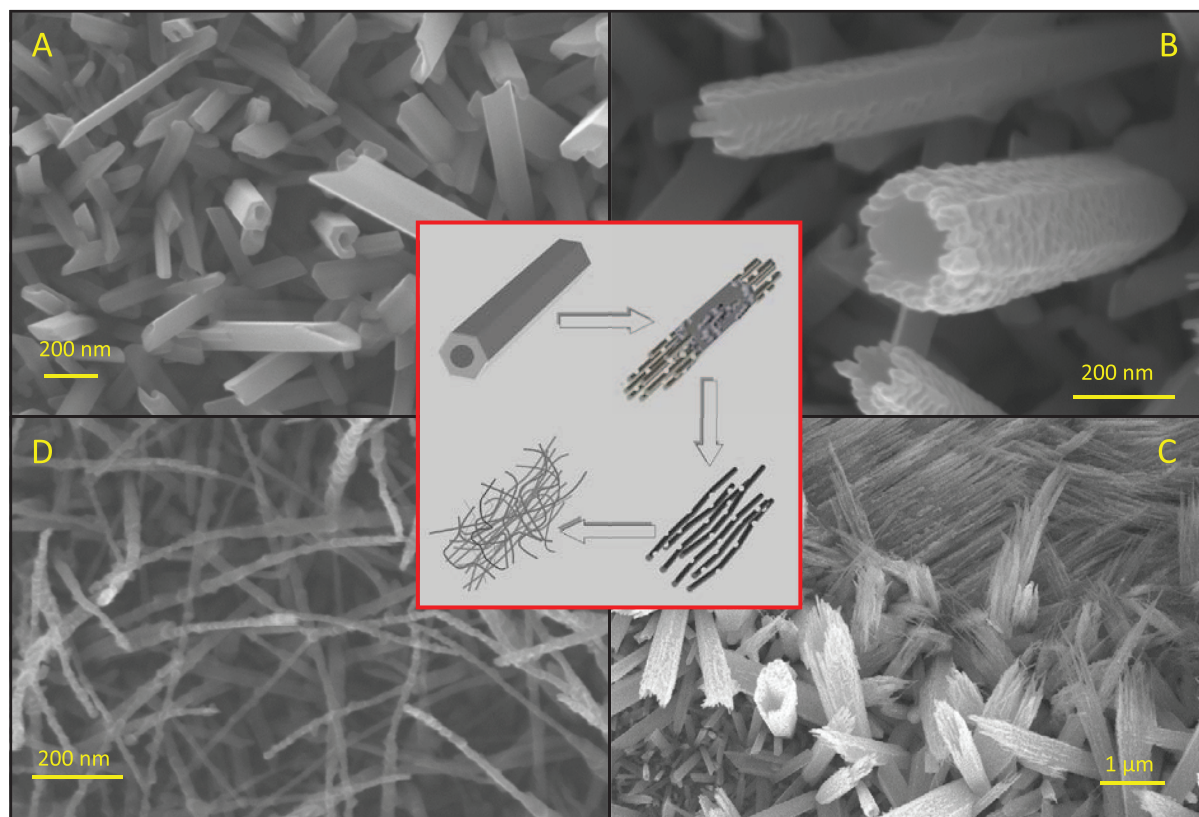


Figure 4 | Progressive controlled photo-induced transformation of *t*-Te NTs to core-Te/sheath-TeO₂ NWs. FESEM images show how neat *t*-Te NTs (A) transform under irradiation to ultrathin NWs (D) which can be either α -TeO₂ and/or Te-core/TeO₂-sheath hybrids. Intermediate steps involve the nanostructuring of the NT surface (B) due to photo-induced oxidation. Oxidation is the key to unzipping the NTs along their long axis. (C) shows intermediate unzipping states towards the final ripping of *t*-Te nanotubes to NWs in (D) with a size distribution in the range 10–20 nm. The roughness of the NWs surface (D) indicates no complete photo-oxidation. The inset shows schematically the *top-down* mechanism of tubes-to-wires transformation.

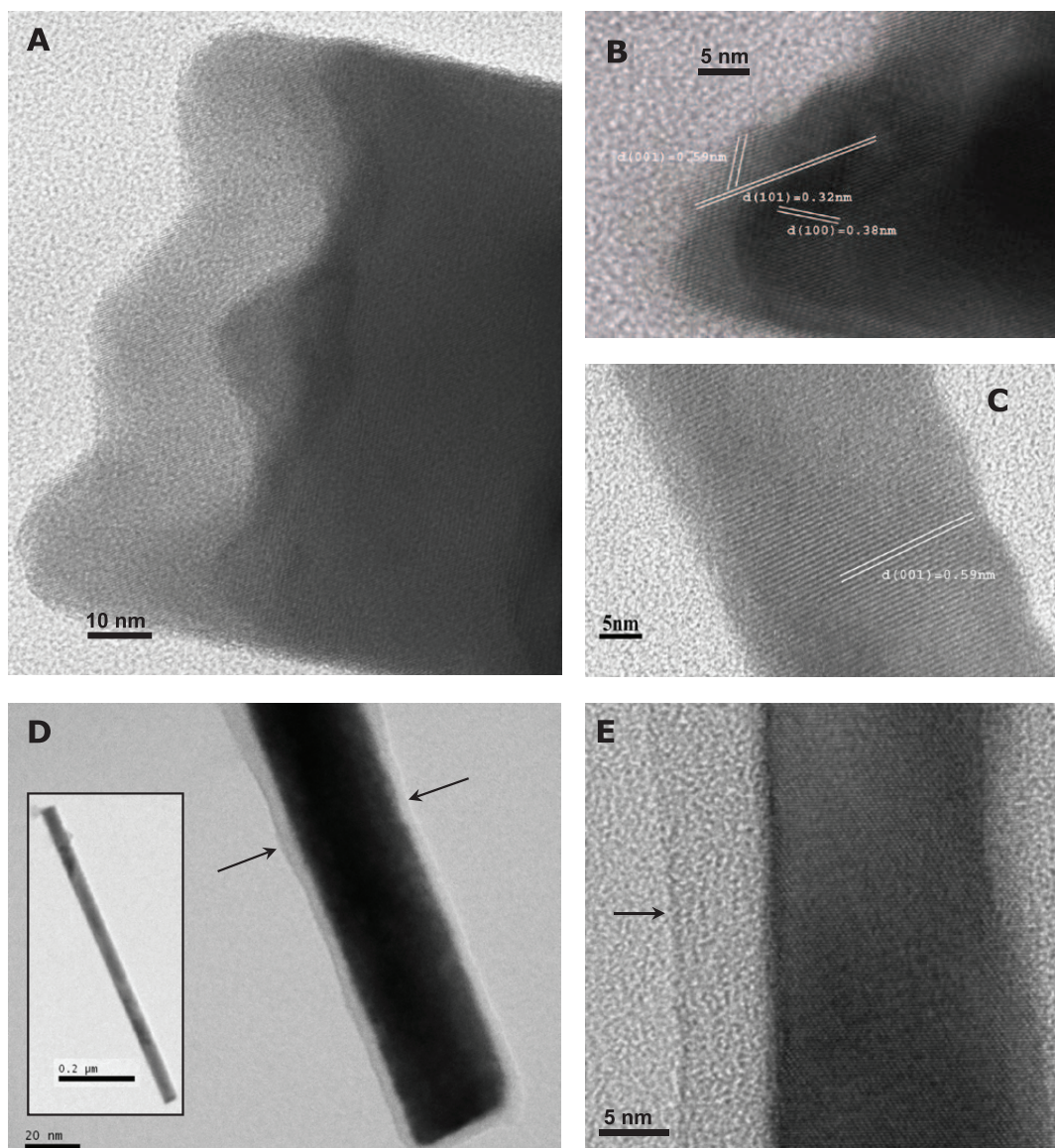


Figure 5 | TEM and HRTEM images of *t*-Te NTs and photo-processed core-Te/sheath-TeO₂ NWs. (A) and (B) TEM image of a *t*-Te nanotube edge and a HRTEM image showing the interplanar spacings, respectively. (C) HRTEM micrograph of a *t*-Te nanowire grown along the [0001] direction. (D) A magnified part of the core-Te/sheath-TeO₂ nanowire. The arrows denote the outer limits of the sheath layer. The width of this layer is of about 3–7 nm. The inset shows the entire nanowire with an aspect ratio of ~25. (E) HRTEM image of a core/sheath structure showing single crystalline *t*-Te coated by an amorphous layer of TeO₂. The arrow shows the outer limits of the amorphous layer.

exploited in microelectronics due to enhanced photoconduction of Te/TeO₂ interfaces in the UV region³⁶.

In summary, we report here a novel, method for the laser-assisted, template-free and surfactant-free fabrication of 1D Te and TeO₂ nanostructures at ambient conditions using visible light. The underlying mechanism combines a bottom-up step for the growth of *t*-Te NTs and a top-down step for the photo-induced ripping of these NTs towards the fabrication of α -TeO₂ nanowires and/or core-Te/sheath-TeO₂ hybrid nanostructures. The vapor-solid mechanism describes the formation of *t*-Te NTs at high fluence, which grow at the periphery of the irradiated area. The second step, namely, photo-oxidation is more complex; its origin was revealed by time-resolved Raman scattering at low fluence conditions. At early stages of irradiation amorphous α -Te and amorphous α -TeO₂ emerge simultaneously, while at prolonged exposure photo-oxidized zones on NTs surface undermine their integrity by an *unzipping effect* along the NT axis. The composition of the NWs formed by NT ripping varies from core-Te/sheath-TeO₂ nano-hybrids to pure TeO₂ nanowires at

longer exposure times. At the fundamental level, we provide solid evidence for the microscopic nature of the observed photo-induced effects. We have shown that photo-amorphization of *t*-Te evolves in parallel with photo-oxidation to α -TeO₂. The current method involves an all-laser, solid state materials processing offering new opportunities for the fast, and spatially controlled fabrication of Te and TeO₂ anisotropic nanomaterials that meet a number of applications in optics, photonics and gas sensing.

Methods

Elemental Te pieces (Alfa Aesar, 6N purity) were polished to optical quality. This is important for achieving uniform focusing of the laser beam for all irradiated points so as to control the laser power density on the surface. Secondary electron images of the irradiated area were obtained with a field emission scanning electron microscope (FE-SEM, Zeiss SUPRA 35VP-FEG). X-ray micro-analysis measurements were carried out with the aid of QUANTAX 200 model unit (Bruker AXS). The O-K_α, and Te-L, Te-M intensities were used to determine atomic concentration profiles. Transmission electron microscope (TEM) and high resolution TEM (HRTEM) images were taken on a JEOL JEM-2100 transmission > electron microscope operated at 200 kV. The



sample for the TEM analysis was prepared by a standard procedure where the nanostructures peeled-off from the TE surface were dispersed in CH₃CH₂OH, by ultrasonic waves and spread onto a carbon-coated copper grid (200 mesh).

Micro-Raman scattering was used to identify the phase changes of Te and TeO₂. The 441.6 nm radiation emerging from a He-Cd laser (Kimon) was used to irradiate *t*-Te and was also acting as the exciting source for recording Raman spectra. The backscattered light was analyzed with the aid of a UV-LabRam (Jobin-Yvon) micro-Raman spectrometer. Spectra were recorded with a single monochromator equipped with CCD camera. Light was focused through a microscope objective (50×) on an area of about 1 μm radius. Neutral density filters were used to control laser beam intensity. Power densities of 10⁵ (D0), 10⁴ (D1), and 10³ (D2) W cm⁻² were selected. The use of a notch filter to eliminate the elastically scattered light prohibited measurements of spectra below ~115 cm⁻¹. Accumulation times were ranging from few seconds to few minutes depending on the power density used.

To identify the presence of TeO₂ phase, selected nanostructures were rinsed with dense (37% per volume) HCl solution and washed with triple distilled water. Being insoluble to HCl solution, elemental Te remained unaffected after this treatment, see Figure S5.

- Xia, Y. *et al.* One-Dimensional Nanostructures: Synthesis, Characterization, and Applications. *Adv. Mater.* **156**, 353–389 (2003).
- Wang, Z. L. ZnO nanowire and nanobelt platform for nanotechnology. *Mater. Sci. Engineer. R* **64**, 33–71 (2009).
- Yang, P. D., Yan, R. & Fardy, M. Semiconductor Nanowire: What's Next? *Nano Lett.* **10**, 1529–1536 (2010).
- Yan, R. *et al.* Nanowire-based single cell endoscopy. *Nature Nanotech.* **7**, 191–196 (2012).
- Furuta, N., Ohasi, Y., Itinose, H. & Igarashi, I. Kinetics of vapor-grown tellurium whiskers. *Jpn. J. Appl. Phys.* **14**, 929–934 (1975).
- Gates, B., Mayers, B., Grossman, A. & Xia, Y. A sonochemical approach to the synthesis of crystalline selenium nanowires in solutions & on solid supports. *Adv. Mater.* **14**, 1749–1752 (2002).
- Mo, M., Zeng, J., Liu, X., Yu, W., Zhang, S. & Qian, Y. Controlled hydrothermal synthesis of thin single-crystal tellurium nanobelts and nanotubes. *Adv. Mater.* **14**, 1658–1662 (2002).
- Gautam, U. K. & Rao, C. N. R. Controlled synthesis of crystalline tellurium nanorods, nanowires, nanobelts and related structures by a self-seeding solution process. *J. Mater. Chem.* **14**, 2530–2535 (2004).
- Tang, Z., Wang, Y., Sun, K. & Kotov, N. A. Spontaneous transformation of stabilizer-depleted binary semiconductor nanoparticles into selenium and tellurium nanowires. *Adv. Mater.* **17**, 358–363 (2005).
- Zhu, H. *et al.* Controlled synthesis of tellurium nanostructures from nanotubes to nanorods and nanowires and their template applications. *J. Phys. Chem. C* **115**, 6375–6380 (2011).
- Zhu, H. *et al.* Controlled hydrothermal synthesis of tri-wing tellurium nanoribbons and their template reaction. *CrystEngComm* **14**, 251–255 (2012).
- Geng, B. Y., Lin, Y., Peng, X. S., Meng, G. W. & Zhang, L. D. Large-scale synthesis of single-crystalline Te nanobelts by a low-temperature chemical vapour deposition route. *Nanotechnology* **14**, 983–986 (2003).
- Mohanty, P., Kang, T., Kim, B. & Park, J. Synthesis of single crystalline tellurium nanotubes with triangular and hexagonal cross sections. *J. Phys. Chem B* **110**, 791–795 (2006).
- Sen, S. *et al.* J. V. Synthesis of tellurium nanostructures by physical vapor deposition and their growth mechanism. *Cryst. Growth Des.* **8**, 238–242 (2008).
- Hawley, C. J., Beatty, B. R., Chen, G. & Spanier, J. E. Shape-controlled vapor-transport growth of tellurium nanowires. *Cryst. Growth Des.* **12**, 2789–2793 (2012).
- Song, J. M. *et al.* Superlong High-Quality Tellurium Nanotubes: Synthesis, Characterization, and Optical Property. *Cryst. Growth Des.* **8**, 1902–1908 (2008).
- Wang, Z. *et al.* Formation of single-crystal tellurium nanowires and nanotubes via hydrothermal recrystallization and their gas sensing properties at room temperature. *J. Mater. Chem.* **20**, 2457–2463 (2010).
- Wei, T. Y., Chang, H. Y., Lee, Y. F., Hung, Y. L. & Huang, C. C. Selective Tellurium Nanowire-based Sensors for Mercury(II) in Aqueous Solution. *J. Chin. Chem. Soc.* **58**, 732–738 (2011).
- Sreepasad, T. S., Samal, A. K. & Pradeep, T. Tellurium nanowire-induced room temperature conversion of graphite oxide to leaf-like graphenic structures. *J. Phys. Chem. C* **113**, 1727–1737 (2009).
- Lin, Z. H., Lee, C. H., Chang, H. Y. & Chang, H. T. Antibacterial activities of tellurium nanomaterials. *Chem. Asian J.* **7**, 930–934 (2012).
- Liang, H. W. *et al.* Ultrathin Te nanowires: An excellent platform for controlled synthesis of ultrathin platinum and palladium nanowires/nanotubes with very high aspect ratio. *Adv. Mater.* **21**, 1850–1854 (2009).
- Jiang, Z. Y. *et al.* Synthesis of α-tellurium dioxide nanorods from elemental tellurium by laser ablation. *Inorg. Chem. Comm.* **7**, 179–181 (2004).
- Liu, Z. *et al.* Room temperature gas sensing of p-type TeO₂ nanowires. *Appl. Phys. Lett.* **90**, 173119.1–173119.3 (2007).
- Kim, S. S. *et al.* Drastic change in shape of tetragonal TeO₂ nanowires and their application to transparent chemical gas sensors. *Appl. Surf. Sci.* **258**, 501–506 (2011).
- Jin, C., Kim, H. & Lee, C. Enhancement of the emission from TeO₂ nanorods by encapsulation with ZnO. *Cryst. Res. Technol.* **46**, 1065–1070 (2011).
- Pine, A. S. & Dresselhaus, G. Raman Spectra and Lattice Dynamics of Tellurium. *Phys. Rev. B* **4**, 356–371 (1971).
- Mirgorodsky, A. P., Merle-Mejean, T., Champarnaud, J. C., Thomas, P. & Frit, B. Dynamics and structure of TeO₂ polymorphs: model treatment of paratellurite and tellurite; Raman scattering evidence for new γ- and δ-phases. *J. Phys. Chem. Solids* **61**, 501–509 (2000).
- Handbook of Optical Constants of Solids, Ed. by E. D. Palik. (Academic, Orlando, 1985).
- Ashitkov, Si. I. *et al.* Ultrafast Laser-Induced Phase Transitions in Tellurium. *JETP Letters* **76**, 461–464 (2002).
- Mayer, B. & Xia, Y. Formation of Tellurium Nanotubes Through Concentration Depletion at the Surfaces of Seeds. *Adv. Mater.* **14**, 279–282 (2002).
- Brodsky, M. H., Gambino, R. J., Smith, J. E. & Yacoby, Y. The Raman Spectrum of Amorphous Tellurium. *Phys. stat. sol. (b)* **52**, 609–614 (1972).
- Yannopoulos, S. N. & Andrikopoulos, K. S. Raman scattering study on structural and dynamical features of noncrystalline selenium. *J. Chem. Phys.* **121**, 4747–4758 (2004).
- Scopigno, T., Steurer, W., Yannopoulos, S. N., Chrissanthopoulos, A., Krisch, M., Ruocco, G. & Wagner, T. Vibrational Dynamics and Surface Structure of Amorphous Materials. *Nature Communications* **2**, Art. No 195 (2011).
- Kolobov, A. V. in *Photo-Induced Metastability in Amorphous Semiconductors*, (Wiley-VCH, Weinheim, Germany 2003).
- Tichy, L., Ticha, H., Nagels, P. & Slecckx, E. A review of the specific role of oxygen in irreversible photo- and thermally induced changes of the optical properties of thin film amorphous chalcogenides. *Opt. Mater.* **4**, 771–779 (1995).
- Oishi, K., Okamoto, K. & Sunada, J. Photoconduction on photo-oxidized tellurium thin films. *Thin Solid Films* **148**, 29–40 (1987).

Acknowledgements

The authors thank Dr. G.A. Voyiatzis (FORTH/ICE-HT) for providing access to the Raman facility.

Author contributions

T.V., V.D., M.K. and S.N.Y. performed experiments and data analysis. S.N.Y. led the research. S.N.Y. and T.V. wrote the manuscript. All authors contributed to the discussion of the manuscript.

Additional information

Supplementary information accompanies this paper at <http://www.nature.com/scientificreports>

Competing financial interests: The authors declare no competing financial interests.

License: This work is licensed under a Creative Commons Attribution-NonCommercial-NoDerivs 3.0 Unported License. To view a copy of this license, visit <http://creativecommons.org/licenses/by-nc-nd/3.0/>

How to cite this article: Vasileiadis, T., Dracopoulos, V., Kollia, M. & Yannopoulos, S.N. Laser-Assisted Growth of *t*-Te Nanotubes and their Controlled Photo-induced Unzipping to ultrathin core-Te/sheath-TeO₂ Nanowires. *Sci. Rep.* **3**, 1209; DOI:10.1038/srep01209 (2013).